Revealing the Nature of Chemical Bonding in an ALn$_2$Ag$_3$Te$_5$-Type Alkaline-Metal (A) Lanthanide (Ln) Silver Telluride

Kai C. Göbgen [1], **Kai S. Fries** [1], **Fabian C. Gladisch** [1], **Richard Dronskowski** [1,2,3] and **Simon Steinberg** [1,*]

[1]   Institute of Inorganic Chemistry, RWTH Aachen University, Landoltweg 1, D-52074 Aachen, Germany;
       kai.goebgen@rwth-aachen.de (K.C.G.); kai.fries@rwth-aachen.de (K.S.F.);
       fabian.gladisch@rwth-aachen.de (F.C.G.); drons@HAL9000.ac.rwth-aachen.de (R.D.)
[2]   Jülich-Aachen Research Alliance (JARA-FIT and -HPC), RWTH Aachen University, Landoltweg 1,
       D-52074 Aachen, Germany
[3]   Hoffmann Institute of Advanced Materials, Shenzhen Polytechnic, 7098 Liuxian Blvd, Nanshan District,
       Shenzhen 518055, China
*   Correspondence: simon.steinberg@ac.rwth-aachen.de; Tel.: +49-241-80-94655

check for updates

Abstract: Although the electronic structures of several tellurides have been recognized by applying the *Zintl-Klemm* concept, there are also tellurides whose electronic structures cannot be understood by applications of the aforementioned idea. To probe the appropriateness of the valence-electron transfers as implied by *Zintl-Klemm* treatments of ALn$_2$Ag$_3$Te$_5$-type tellurides (A = alkaline-metal; Ln = lanthanide), the electronic structure and, furthermore, the bonding situation was prototypically explored for RbPr$_2$Ag$_3$Te$_5$. The crystal structure of that type of telluride is discussed for the examples of RbLn$_2$Ag$_3$Te$_5$ (Ln = Pr, Nd), and it is composed of tunnels which are assembled by the tellurium atoms and enclose the rubidium, lanthanide, and silver atoms, respectively. Even though a *Zintl-Klemm* treatment of RbPr$_2$Ag$_3$Te$_5$ results in an (electron-precise) valence-electron distribution of (Rb$^+$)(Pr^{3+})$_2$(Ag$^+$)$_3$(Te^{2-})$_5$, the bonding analysis based on quantum-chemical means indicates that a full electron transfer as suggested by the *Zintl-Klemm* approach should be considered with concern.

1. Introduction

The understanding and, furthermore, the tailored design of the physical properties for a given solid-state material requires a proper knowing of its electronic (band) structure [1,2]. In addition, the knowledge of the total (electronic) energy, which is evaluated from the electronic (band) structure computations for a given material, also provides valuable information about the structural preferences and, hence, stability trends for such a substance [3,4]. The total energy of a given material depends on two elementary energetic contributions, that are, the site energy and the bond energy [2]. Although the energy arising from the bonds within a given solid-state material plays an important role with regard to its total energy, the interpretation of the nature of bonding has still remained challenging for one particular class of solid-state materials, i.e., intermetallic phases [5]. Yet, certain concepts, e.g., those stated by *Hume-Rothery* [6–8] or *Zintl* and *Klemm* [9–11], help to understand the distributions of valence-electrons in some intermetallics. On the other hand, more recent research [1,12] on polar intermetallic compounds revealed the existence of polyanionic or polycationic units ("clusters") which are combined with monoatomic counterions, but are electron-poorer relative to Zintl phases.

Among the group of intermetallic compounds, tellurides have attracted an enormous interest because of the employments as materials for diverse applications including thermoelectric energy conversion [13–15] or data storage [16–18]. The distributions of the valence-electrons in the tellurides have been typically described by applying the *Zintl-Klemm* concept [19,20]; however, the application of the latter to certain tellurides containing low-dimensional tellurium fragments resulted in the assignments of non-electron-precise charges to the tellurium atoms [20]. In that connection, recent research [21,22] on the electronic structures of certain tellurides, i.e., $LaCu_xTe_2$ ($0.28 \leq x \leq 0.50$), $Gd_3Cu_2Te_7$, and $Ag_{5-x}Te_3$ ($-0.25 \leq x \leq 1.44$), indicated that the valence-electron transfers as suggested by *Zintl-Klemm* treatments should be taken with a grain of salt. In fact, analyzing the nature of bonding for the aforementioned tellurides revealed the presence of strong rare-earth–tellurium as well as transition-metal–tellurium bonding interactions being in stark contrast to the (complete) valence-electron transfers as assumed by *Zintl-Klemm* treatments. The outcome of these examinations stimulated our impetus to determine the electronic structures and, furthermore, the nature of bonding for tellurides, which are expected to comprise rather ionic interactions, but also the aforementioned mixed-metal interactions.

In the quest for tellurides, which are estimated to show rather ionic as well as mixed-metal interactions, the group of the quaternary alkaline-metal rare-earth transition-metal tellurides has attracted our interest. Previous research on the group of the quaternary tellurides has focused on exploring the formations [23,24] of charge density waves, the effectiveness [25–28] for thermoelectric energy conversion, and the magnetic [29] properties. In this contribution, we examine the electronic structure and, furthermore, the nature of bonding for one representative of the $ALn_2Ag_3Te_5$-type (A = alkaline-metal; Ln = lanthanide), whose crystal structure will be described for the examples of $RbLn_2Ag_3Te_5$ (Ln = Pr, Nd).

2. Results and Discussion

The quaternary $RbLn_2Ag_3Te_5$ (Ln = Pr, Nd; Table 1) were obtained as high-yield products from reactions of the respective lanthanides, silver, and tellurium in the presence of rubidium chloride, which was used as a reactive flux [30] (see Section 3.1). Both tellurides are isostructural to the recently reported [28] $RbLn_2Ag_3Te_5$ (Ln = Sm, Gd–Dy), which are related to smaller unit cell volumes relative to the herein reported tellurides as a consequence of the lanthanide contraction [31]. A comparison of the unit cell volumes of $RbLn_2Ag_3Te_5$ (Ln = Pr, Nd; Table 1) to those of the cesium-containing analogues [28], i.e., $CsLn_2Ag_3Te_5$ (Ln = Pr, Nd), reveals that the unit cells of the rubidium-containing tellurides are smaller because of an increased atomic radius [32] from rubidium (2.20 Å) to cesium (2.44 Å). To provide an insight into the structural features for this type of telluride, the crystal structures of the quaternary $RbLn_2Ag_3Te_5$ (Ln = Pr, Nd) will be inspected in detail in the following.

2.1. Structural Details

$RbLn_2Ag_3Te_5$ (Ln = Pr, Nd) crystallize with the orthorhombic space group *Cmcm* (Tables 1 and 2) and their crystal structures are composed of one-dimensional tunnels (Figure 1), which are assembled by the tellurium atoms and enclose the rubidium, silver, and lanthanide atoms. More specifically, the rubidium atoms reside in the centers of bicapped trigonal tellurium prisms, $[Rb@Te_8]$, that are condensed via their triangular faces to linear $^1_\infty[Rb@Te_8]$ chains parallel to the *a*-axis. Each $[Rb@Te_8]$ unit shares six edges with six nearest neighboring tellurium octahedra enclosing the lanthanide atoms, $[Ln@Te_6]$. The $[Ln@Te_6]$ units are connected via common edges to $^1_\infty[Ln@Te_6]$ double chains, while the silver atoms occupy the tetrahedral voids located between the $^1_\infty[Rb@Te_8]$ chains and $^1_\infty[Ln@Te_6]$ double chains. The tetrahedral $[Ag@Te_4]$ units encapsulating the Ag5 atoms (Wyckoff position 8*f*) join edges and vertices with neighboring $[Ag5@Te_4]$ units to construct $^1_\infty[Ag5@Te_4]$ double chains parallel to the *a*-axis. Additionally, the tellurium tetrahedra encompassing the Ag6 atoms (Wyckoff position 4*c*), $[Ag6@Te_4]$, are connected via common tellurium atoms to neighboring units within the $^1_\infty[Ag6@Te_4]$ chains as well as nearby $^1_\infty[Ag5@Te_4]$ double chains. A closer topological inspection of the $^1_\infty[Ag5@Te_4]$

double chains reveals the presence of relatively short Ag5–Ag5 contacts (see Table 3). Considering the covalent atomic radii [32] of silver (1.45 Å), such short Ag–Ag separations of ~2.95 Å suggest the presence of Ag–Ag bonding interactions; however, an application of the *Zintl-Klemm* concept [9–11] to $RbLn_2Ag_3Te_5$ (Ln = Pr, Nd) leads to a formal (electron-precise) valence-electron-distribution of $(Rb^+)(Ln^{3+})_2(Ag^+)_3(Te^{2-})_5$ disregarding the presence of Ag–Ag bonds. To determine the actual nature of bonding for this telluride, we followed up with a prototypical examination of the electronic band structure for $RbPr_2Ag_3Te_5$.

Table 1. Details of the crystal structure investigations and refinements for $RbLn_2Ag_3Te_5$ (Ln = Pr, Nd).

Formula	$RbPr_2Ag_3Te_5$	$RbNd_2Ag_3Te_5$
from wt.	1328.90	1335.56
space group	*Cmcm* (no. 63)	
a (Å)	4.618(2)	4.607(2)
b (Å)	16.014(7)	16.031(7)
c (Å)	18.644(8)	18.594(8)
volume (Å^3)	1378.7(10)	1373.1(10)
Z	4	
density (calc.), g/cm^3	6.402	6.461
μ (mm^{-1})	24.946	25.513
F (000)	2224	2232
θ range (°)	2.19–25.76	2.19–25.67
index ranges	$-5 \leq h \leq 5$	$-5 \leq h \leq 5$
	$-18 \leq k \leq 19$	$-19 \leq k \leq 18$
	$-22 \leq l \leq 22$	$-20 \leq l \leq 22$
reflections collected	4203	3900
independent reflections	774	762
refinement method	full-matrix least-squares on F^2	
data/restraints/parameters	774/0/37	762/0/37
goodness-of-fit on F^2	1.16	1.15
final R indices [$I > 2\sigma(I)$]	$R_1 = 0.036$; $wR_2 = 0.081$	$R_1 = 0.066$; $wR_2 = 0.156$
R indices (all data)	$R_1 = 0.040$; $wR_2 = 0.082$	$R_1 = 0.068$; $wR_2 = 0.158$
R_{int}	0.068	0.098
largest diff. peak and hole, e$^-$/Å^3	1.99 and -3.90	3.25 and -6.84

Table 2. Atomic positions and equivalent anisotropic displacement parameters for $RbPr_2Ag_3Te_5$ and $RbNd_2Ag_3Te_5$.

Atom	Position	x	y	z	U_{eq}, Å^2
			$RbPr_2Ag_3Te_5$		
Pr1	8*f*	0	0.3096(1)	0.5945(1)	0.0114(2)
Te2	8*f*	1/2	0.4421(1)	0.6232(1)	0.0124(3)
Te3	8*f*	0	0.3289(1)	0.4264(1)	0.0110(3)
Te4	4*c*	0	0.2389(1)	3/4	0.0128(3)
Ag5	8*f*	0	0.0864(1)	0.5275(1)	0.0208(3)
Ag6	4*c*	1/2	0.3360(1)	3/4	0.0229(4)
Rb7	4*c*	0	0.5587(1)	3/4	0.0227(5)
			$RbNd_2Ag_3Te_5$		
Nd1	8*f*	0	0.3095(1)	0.5945(1)	0.0071(4)
Te2	8*f*	1/2	0.4417(1)	0.6230(1)	0.0084(4)
Te3	8*f*	0	0.3281(1)	0.4265(1)	0.0071(4)
Te4	4*c*	0	0.2390(1)	3/4	0.0082(5)
Ag5	8*f*	0	0.0865(1)	0.5281(1)	0.0161(5)
Ag6	4*c*	1/2	0.3359(2)	3/4	0.0185(6)
Rb7	4*c*	0	0.5587(2)	3/4	0.0182(7)
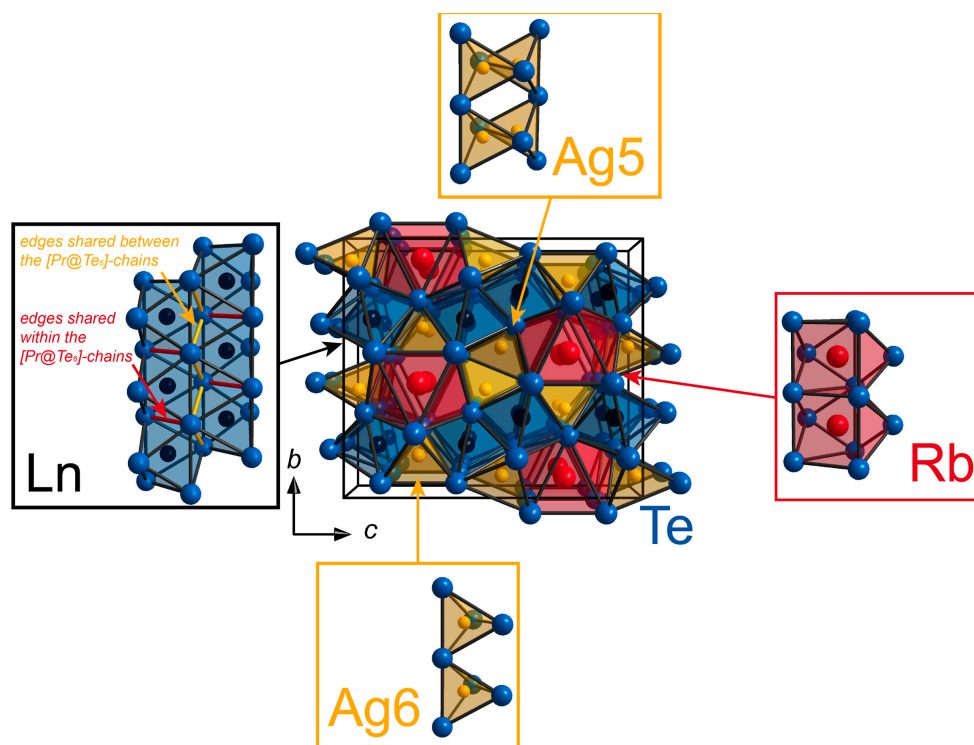
Figure 1. View on the unit cell of $RbLn_2Ag_3Te_5$ (Ln = Pr, Nd) along *a*: the crystal structures of the tellurides are composed of tunnels which are assembled by the tellurium atoms and enclose the rubidium, lanthanide, and silver atoms, respectively. The diverse types of tellurium (blue) polyhedra surrounding the rubidium (red), lanthanide (black), and silver atoms (orange) are shown in the insets.

Table 3. Distances, numbers of bonds, –ICOHP/bond values, average –ICOHP/bond values, cumulative –ICOHP/cell, and percentage contributions to the net bonding capability of the diverse contacts in $RbPr_2Ag_3Te_5$.

Interaction	Distance (Å)	No. of Bonds	–ICOHP/bond (eV/bond)	Ave. –ICOHP/bond (eV/bond)	Cum. –ICOHP/cell	%
Pr1-Te2	3.182(1)	16	1.103			
Pr1-Te3	3.150(2)	8	1.363			
Pr1-Te3	3.225(1)	16	0.936	1.123	53.892	43.7
Pr1-Te4	3.112(2)	8	1.295			
Rb7-Te2	3.796(2)	16	0.045			
Rb7-Te3	3.749(2)	8	0.038	0.045	1.425	1.1
Rb7-Te4	3.696(2)	8	0.050			
Ag5-Ag5	2.952(2)	4	0.455	0.455	1.819	1.5
Ag5-Te2	2.846(2)	8	1.385			
Ag5-Te2	2.919(2)	8	0.930			
Ag5-Te3	2.812(1)	16	1.412	1.381	66.265	53.7
Ag6-Te2	2.913(2)	8	1.323			
Ag6-Te4	2.783(2)	8	1.821			

2.2. Electronic Structure and Chemical Bonding Analysis

An examination of the densities-of-states (DOS) curves for $RbPr_2Ag_3Te_5$ (Figure 2) reveals that the occupied states close to the Fermi level, E_F, originate to a large extent from the Ag-*d* and Te-*p* atomic orbitals beside minor contributions from the Pr-*d* states. This outcome implies that the majority of the valence electrons and, hence, bonding interactions reside between the Ag–Te, Pr–Te, and Ag–Ag contacts. A further integration of the energy regions near E_F also bares that the contributions arising from the Rb-*s* bands are rather negligible (not shown in Figure 2). Accordingly, one may infer that

rubidium acts as a one-electron donor in the telluride. Because the Fermi level in RbPr$_2$Ag$_3$Te$_5$ falls in a band gap of 0.93 eV, an electronically favorable situation is achieved for this telluride. Furthermore, the presence of the band gap at the Fermi level is in full accordance with the formal valence-electron distribution as proposed by the application of the *Zintl-Klemm* concept. Yet, there are the Ag–Ag separations of ~2.95 Å suggesting the presence of Ag–Ag bonding interactions which are not predicted by a *Zintl-Klemm* treatment.

To provide an insight into the bonding situation in RbPr$_2$Ag$_3$Te$_5$, we followed up with an examination of the crystal orbital Hamilton population curves (COHP; Figure 2) and their respective integrated values (Table 3). In this context, the cumulative –ICOHP/cell values, i.e., the sums of the negative ICOHP/bond values of all nearest neighboring contacts within one unit cell, were projected as percentages of the net bonding capabilities for each sort of interaction to identify roles of the diverse interactions in overall bonding—a procedure that has been largely employed elsewhere [21,22,33–36].

A comparison of all –ICOHP/bond values bares that the largest values correspond to the heteroatomic Pr–Te and Ag–Te interactions, which contribute 43.7% (Pr–Te) and 53.7% (Ag–Te) to the total bonding capabilities. Therefore, it may be concluded that the vast majority of the bonding populations is located between the Pr–Te and Ag–Te interactions. The Rb–Te interactions are related to rather small –ICOHP/bond values, which contribute 1.1% to the net bonding capabilities. Under consideration of previous research [37,38] on the electronic structures of alkaline-metal-containing polar intermetallics, this outcome suggests that the Rb–Te interactions should be considered as ionic interactions, while the Pr–Te and Ag–Te interactions should be regarded as rather strong, polar, mixed-metal bonds. This outcome also indicates that a full valence-electron transfer as proposed by an application of the *Zintl-Klemm* concept should be regarded with suspicion—a consequence which has also been identified by recent explorations of the electronic structures of rare-earth transition-metal tellurides [22] as well as silver tellurides [21]. The homoatomic Ag–Ag interactions change from bonding to considerable antibonding states at −4.41 eV, which may be regarded as attributes of the d^{10}–d^{10} closed-shell [39,40] interactions; however, the Ag–Ag –ICOHP values are indicative of a net bonding character for these interactions. Because of the rather low bond frequency of the Ag–Ag separations, these interactions solely contribute 1.5% to the net bonding capabilities.
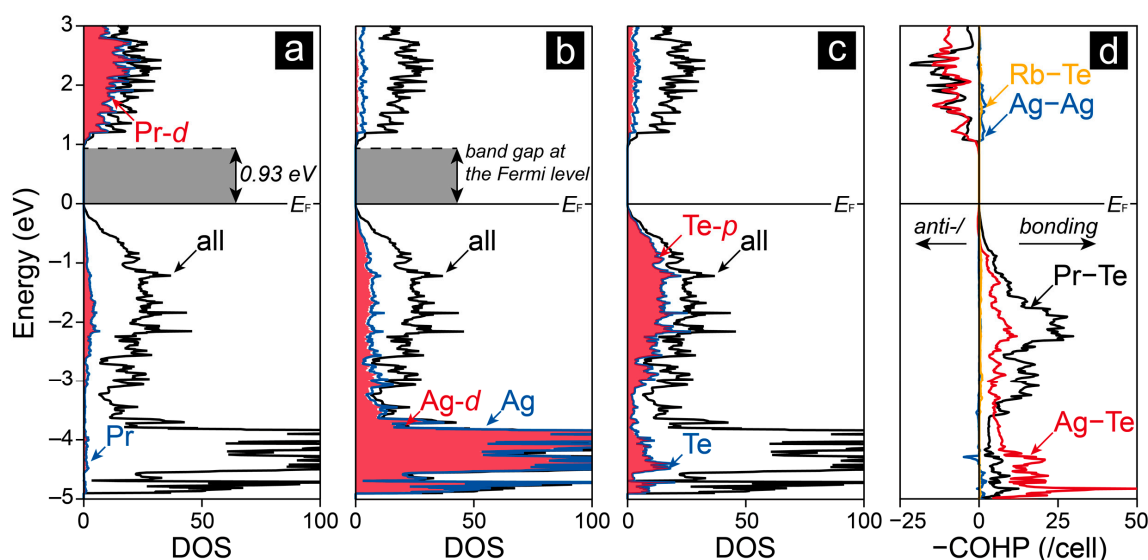

Figure 2. Densities-of-states (DOS) and crystal orbital Hamilton population (COHP) curves of RbPr$_2$Ag$_3$Te$_5$: the Fermi level, E_F, is given by the black horizontal line, while the atom-projected DOS (blue) of praseodymium, silver, and tellurium are shown in (**a**)–(**c**), respectively. Additionally, the orbital-projected DOS (red) which provide the largest contributions to the states near E_F for a given sort of atom have been included.

3. Materials and Methods

3.1. Syntheses

　　　RbLn$_2$Ag$_3$Te$_5$ (Ln = Pr, Nd) were obtained from reactions of the respective rare-earth-elements (smart-elements®, Vienna, Austria, Pr: 99.9%, Nd: 99.9%), silver (Alfa®, Haverhill, MA, USA, ≥99.99%), and tellurium (Merck®, Darmstadt, Germany, >99%) in the presence of rubidium chloride (Sigma Aldrich®, St. Louis, MO, USA, 99.8%), which was employed as a reactive [30] flux. Powders of the rare-earth elements were obtained from filing large ingots, whose surfaces were polished prior to every use. All reactants were stored and handled in an argon-filled glove box with strict exclusion of air and moisture (MBraun®, Garching, Germany; O$_2$ < 0.1 ppm by volume; H$_2$O < 0.3 ppm by volume). In the glove box, mixtures of 0.3 mmol Ln, 0.45 mmol Ag, 0.75 mmol Te, and 0.5 mmol RbCl were first weighed, then pesteled and, finally, loaded in one-side-closed silica tubes, which were subsequently flame-sealed under a dynamic vacuum of at least 2 × 10^{-3} mbar. The samples were heated using computer-controlled tube furnaces and the following temperature program: heat to 400 °C in 5 h, slowly warm up to 850 °C with a rate of 10 °C/h, keep that temperature for 100 h, slowly cool to 300 °C with a rate of 2 °C/h, and equilibrate to room temperature within 25 h. The excess flux was removed with the aid of deionized water, and the products appeared as grey powders containing small crystals. Phase analyses based on powder X-ray diffraction techniques (see Figure 3 and Section 3.2) revealed that the products, which remained stable in air for at least two weeks, were obtained in high yields. Further research, which has been conducted under similar conditions and started from the reactants holmium, silver, tellurium, and a RbCl/LiCl flux, resulted in the identification of the respective holmium-containing telluride (*a* = 4.52(1) Å; *b* = 16.14(4) Å; *c* = 18.30(4) Å).
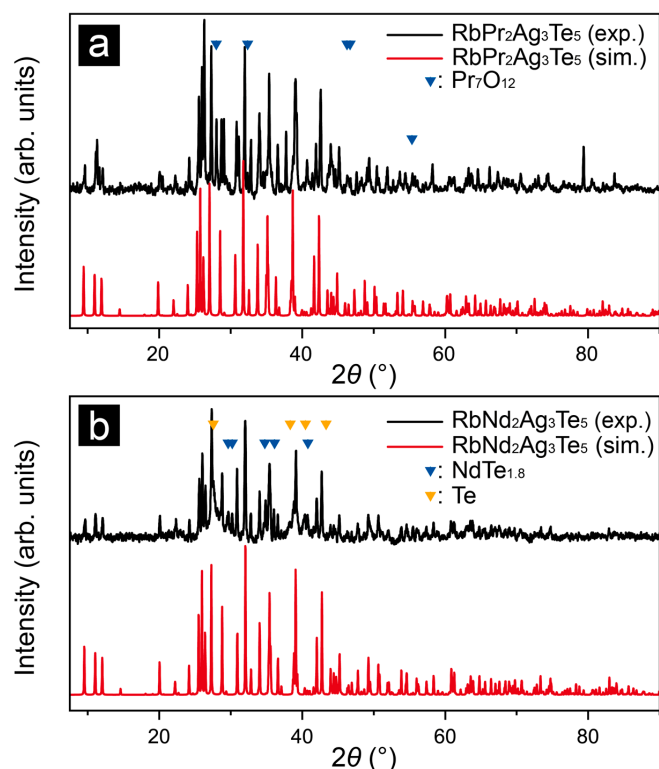

Figure 3. Measured and simulated powder X-ray diffraction patterns of (**a**) RbPr$_2$Ag$_3$Te$_5$ and (**b**) RbNd$_2$Ag$_3$Te$_5$: reflections corresponding to the by-products, i.e., Pr$_7$O$_{12}$ [41], NdTe$_{1.8}$ [42,43], and tellurium [44], have been denoted by the different triangles.

3.2. X-ray Diffraction Studies and Determinations of the Crystal Structures

Sets of powder X-ray diffraction (PXRD) data were collected to identify the yields of $RbLn_2Ag_3Te_5$ (Ln = Pr, Nd) and feasible side-products by comparing the measured PXRD patterns to those which were simulated for $RbLn_2Ag_3Te_5$ (Ln = Pr, Nd) and plausible side-products. To measure the samples, the obtained products were first finely ground and, then, dispersed on Mylar sheets with grease, which were fixed between split aluminum rings. The sets of PXRD data were collected at room temperature with the aid of a STOE StadiP diffractometer (Stoe® & Cie, Darmstadt, Germany; area detector; Cu Kα radiation; λ = 1.54059 Å). The WinXPow software package [45] was utilized for control of the measurements and further processing of the measured PXRD patterns, while phase analyses were conducted using the Match! [46] code.

For the collections of the sets of single-crystal X-ray intensity data, samples were selected from the bulk, mounted on capillaries with grease and, finally, transferred to a Bruker APEX CCD diffractometer (Bruker Inc.®, Madison, WI, USA; Mo Kα radiation; λ = 0.71073 Å). The diffractometer was employed for initial inspections of the quality of the samples and the collections of the X-ray intensity data at room temperature. The programs SAINT+ and SADABS [47] were employed for the integrations of the raw X-ray intensity data and multi-scan absorption corrections, respectively. Applications of the reflection conditions to the collected X-ray intensity data were accomplished with the XPREP [48] algorithms and indicated space group *Cmcm* (no. 63) for both tellurides. The structures were solved using direct methods (SHELXS-97 [49]) in the aforementioned space group, while the structure refinements, which also included anisotropic atomic displacement parameters for all sites, were carried out in full matrix least-squares on F^2 with the SHELXL-2014 [49,50] code. CCDC 1911953 and 1911960 contain the crystallographic data for this paper (see Supplementary Materials). These data can also be obtained free of charge via http://www.ccdc.cam.ac.uk/conts/retrieving.html or from the CCDC, 12 Union Road, Cambridge CB2 1EZ, UK; Fax: +44-1223-336033; E-Mail: deposit@ccdc.cam.ac.uk.

3.3. Computational Details

Full structural optimizations (lattice parameters and atomic positions) and electronic band structure computations for $RbPr_2Ag_3Te_5$ were accomplished utilizing the projector augmented wave (PAW) method [51] as implemented in the Vienna ab initio Simulation Package [52–56] (VASP). Correlation and exchange were depicted by the generalized gradient approximation of Perdew, Burke, and Ernzerhof (GGA–PBE [57]), while the energy cutoff of the plane-wave basis set was 500 eV and a mesh of 12 × 3 × 3 k-points was used to sample the first Brillouin zone. All computations were considered converged once the energy differences between two iterative steps of the electronic (and ionic) relaxations fell below 10^{-8} (and 10^{-6}) eV/cell.

A chemical bonding analysis of $RbPr_2Ag_3Te_5$ was accomplished based on the crystal orbital Hamilton population (COHP [36,58]) method, in which the off-site projected DOS are weighted with the respective Hamilton matrix elements to identify bonding, non-bonding, and antibonding interactions. The COHP curves and the corresponding integrated values (ICOHP) were computed utilizing the tight-binding linear-muffin-tin orbital (TB-LMTO) method in the atomic sphere approximation (ASA) [59–61] and employing the von Barth-Hedin [62] exchange-correlation functional. The Wigner-Seitz (WS) radii were automatically generated, while empty spheres were included to accomplish optimal approximations of full potentials. The following orbitals were employed as basis sets in the computations (downfolded [63] orbitals in parentheses): Rb-5*s*/(-5*p*)/(-4*d*)/(-4*f*); Pr-6*s*/(-6*p*)/-5*d*; Ag-5*s*/-5*p*/-4*d*/(-4*f*); Te-5*s*/-5*p*/(-5*d*)/(-4*f*) with the corresponding WS radii (Å): Rb, 4.73; Pr, 3.58; Ag, 2.86–2.89; Te, 3.24–3.35. The praseodymium 4*f* states were treated as core-like states—a procedure that has been widely used elsewhere [34,35,64,65]. More specifically, the aforementioned handling of the rare-earth-metal 4*f* states has been substantiated by previous explorations [34,35,65–67] on the electronic structures of rare-earth-containing compounds. Namely, the bands corresponding to the rare-earth-metal 4*f* atomic orbitals are typically related to modest dispersions and, hence, are rather

localized such that these states scarcely participate in overall bonding. Reciprocal space integrations were achieved employing the tetrahedron method [68] with a $12 \times 12 \times 6$ k-points set.

4. Conclusions

The appropriateness of valence-electron transfers as proposed by *Zintl-Klemm* treatments has been probed for tellurides which crystallize with the $ALn_2Ag_3Te_5$-type of structure (A = alkaline-metal; Ln = lanthanide). The crystal structure of that type of telluride has been described for the examples of the previously unknown $RbLn_2Ag_3Te_5$ (Ln = Pr, Nd) containing tunnels which are constituted by the tellurium atoms and encapsulate the rubidium, lanthanide, and silver atoms, respectively. Although an application of the *Zintl-Klemm* concept to $RbLn_2Ag_3Te_5$ (Ln = Pr, Nd) leads to an electron-precise valence-electron distribution of $(Rb^+)(Ln^{3+})_2(Ag^+)_3(Te^{2-})_5$, yet, the bonding analysis based on the COHP method indicates that a full electron transfer as suggested by such a *Zintl-Klemm* treatment should be considered with concern. In fact, the majority of the bonding population is located between the Pr–Te and Ag–Te contacts showing characteristics of strong, polar mixed-metal bonds, while the Rb–Te interactions may be regarded as rather ionic bonds. Even though the Ag–Ag interactions change from bonding to antibonding states below the Fermi level as a consequence of closed-shell interactions, an integration of the –COHP curves for these homoatomic interactions indicates a net bonding character.

Author Contributions: K.C.G., K.S.F., and F.C.G. conducted the syntheses, while the crystal structure solutions and refinements were carried out by K.C.G.; S.S. accomplished the electronic structure computations, independently designed and supervised the project. The manuscript was written with input from all authors (K.C.G., K.S.F., F.C.G., R.D., and S.S.), who approved the final version of the manuscript.

Conflicts of Interest: The authors declare no conflict of interest.

References

1. Gladisch, F.C.; Steinberg, S. Revealing Tendencies in the Electronic Structures of Polar Intermetallic Compounds. *Crystals* **2018**, *8*, 80. [CrossRef]
2. Miller, G.J. The "Coloring Problem" in Solids: How It Affects Structure, Composition and Properties. *Eur. J. Inorg. Chem.* **1998**, *1998*, 523–536. [CrossRef]
3. Gautier, R.; Zhang, X.; Hu, L.; Yu, L.; Lin, Y.; Sunde, T.O.L.; Chon, D.; Poeppelmeier, K.R.; Zunger, A. Prediction and accelerated laboratory discovery of previously unknown 18-electron ABX compounds. *Nat. Chem.* **2015**, *7*, 308–316. [CrossRef]
4. Curtarolo, S.; Hart, G.L.W.; Nardelli, M.B.; Mingo, N.; Sanvito, S.; Levy, O. The high-throughput highway to computational materials design. *Nat. Mater.* **2013**, *12*, 191–201. [CrossRef] [PubMed]
5. Nesper, R. Bonding Patterns in Intermetallic Compounds. *Angew. Chem. Int. Ed. Engl.* **1991**, *30*, 789–817. [CrossRef]
6. Jones, H. The phase boundaries in binary alloys, part 2: The theory of the α, β phase boundaries. *Proc. Phys. Soc.* **1937**, *49*, 250–257. [CrossRef]
7. Massalski, T.B.; Mizutani, U. Electronic Structure of Hume-Rothery Phases. *Prog. Mater. Sci.* **1978**, *22*, 151–262. [CrossRef]
8. Mizutani, U.; Sato, H. The Physics of the Hume-Rothery Electron Concentration Rule. *Crystals* **2017**, *7*, 9. [CrossRef]
9. Zintl, E. Intermetallische Verbindungen. *Angew. Chem.* **1939**, *52*, 1–6. [CrossRef]

10. Schäfer, H.; Eisenmann, B.; Müller, W. Zintl Phases: Transitions between Metallic and Ionic Bonding. *Angew. Chem. Int. Ed.* **1973**, *12*, 694–712. [CrossRef]

11. Miller, G.J.; Schmidt, M.W.; Wang, F.; You, T.-S. Quantitative Advances in the Zintl-Klemm Formalism. In *Structure and Bonding*; Fässler, T., Ed.; Springer Publishers: Berlin/Heidelberg, Germany, 2011; Volume 139, pp. 1–55.

12. Corbett, J.D. Exploratory Synthesis: The Fascinating and Diverse Chemistry of Polar Intermetallic Phases. *Inorg. Chem.* **2010**, *49*, 13–28. [CrossRef] [PubMed]

13. Toberer, E.S.; May, A.F.; Snyder, G.J. Zintl Chemistry for Designing High Efficiency Thermoelectric Materials. *Chem. Mater.* **2010**, *22*, 624–634. [CrossRef]

14. Snyder, G.J.; Toberer, E.S. Complex thermoelectric materials. *Nat. Mater.* **2008**, *7*, 105–114. [CrossRef] [PubMed]

15. Sootsman, J.R.; Chung, D.Y.; Kanatzidis, M.G. New and Old Concepts in Thermoelectric Materials. *Angew. Chem. Int. Ed.* **2009**, *48*, 8616–8639. [CrossRef] [PubMed]

16. Wuttig, M.; Yamada, N. Phase-change materials for rewriteable data storage. *Nat. Mater.* **2007**, *6*, 824–832. [CrossRef] [PubMed]

17. Lencer, D.; Salinga, M.; Grabowski, B.; Hickel, T.; Neugebauer, J.; Wuttig, M. A map for phase-change materials. *Nat. Mater.* **2008**, *7*, 972–977. [CrossRef]

18. Wuttig, M.; Raoux, S. The Science and Technology of Phase Change Materials. *Z. Anorg. Allg. Chem.* **2012**, *638*, 2455–2465. [CrossRef]

19. Böttcher, P. Tellurium-Rich Tellurides. *Angew. Chem. Int. Ed. Engl.* **1988**, *27*, 759–772. [CrossRef]

20. Papoian, G.A.; Hoffmann, R. Hypervalent Bonding in One, Two, and Three Dimensions: Extending the Zintl-Klemm Concept to Nonclassical Electron-Rich Networks. *Angew. Chem. Int. Ed.* **2000**, *39*, 2408–2448. [CrossRef]

21. Göbgen, K.C.; Gladisch, F.C.; Steinberg, S. The Mineral Stützite: a Zintl-Phase or Polar Intermetallic? A Case Study Using Experimental and Quantum-Chemical Techniques. *Inorg. Chem.* **2018**, *57*, 412–421. [CrossRef]

22. Gladisch, F.C.; Steinberg, S. Revealing the Nature of Bonding in Rare-Earth Transition-Metal Tellurides by Means of Methods Based on First Principles. *Eur. J. Inorg. Chem.* **2017**, *2017*, 3395–3400. [CrossRef]

23. Malliakas, C.D.; Kanatzidis, M.G. Charge Density Waves in the Square Nets of Tellurium of *AMRE*Te$_4$ (*A* = K, Na; *M* = Cu, Ag; *RE* = La, Ce). *J. Am. Chem. Soc.* **2007**, *129*, 10675–10677. [CrossRef]

24. Patschke, R.; Heising, J.; Kanatzidis, M.; Brazis, P.; Kannewurf, C.R. KCuCeTe$_4$: A New Intergrowth Rare Earth Telluride with an Incommensurate Superstructure Associated with a Distorted Square Net of Tellurium. *Chem. Mater.* **1998**, *10*, 695–697. [CrossRef]

25. Patschke, R.; Brazis, P.; Kannewurf, C.R.; Kanatzidis, M. K$_2$Ag$_3$CeTe$_4$: A Semiconducting Tunnel Framework Made from the Covalent "Link-Up" of [Ag$_2$CeTe$_4$]$^{3-}$ Layers with Ag. *Inorg. Chem.* **1998**, *37*, 6562–6563. [CrossRef]

26. Patschke, R.; Brazis, P.; Kannewurf, C.R.; Kanatzidis, M. Rb$_2$Cu$_3$CeTe$_5$: A quaternary semiconducting compound with a two-dimensional polytelluride framework. *J. Mater. Chem.* **1998**, *8*, 2587–2589. [CrossRef]

27. Meng, C.-Y.; Chen, H.; Wang, P.; Chen, L. Syntheses, Structures, and Magnetic and Thermoelectric Properties of Double-Tunnel Tellurides: A$_x$RE$_2$Cu$_{6-x}$Te$_6$ (A = K–Cs; RE = La–Nd). *Chem. Mater.* **2011**, *23*, 4910–4919. [CrossRef]

28. Meng, C.-Y.; Chen, H.; Wang, P. Syntheses, Structures, and Physical Properties of CsRE$_2$Ag$_3$Te$_5$ (RE = Pr, Nd, Sm, Gd–Er) and RbRE$_2$Ag$_3$Te$_5$ (RE = Sm, Gd–Dy). *Inorg. Chem.* **2014**, *53*, 6893–6903. [CrossRef]

29. Babo, J.-M.; Choi, E.S.; Albrecht-Schmitt, T.E. Synthesis, Structure, Magnetism, and Optical Properties of Cs$_2$Cu$_3$DyTe$_4$. *Inorg. Chem.* **2012**, *51*, 11730–11735. [CrossRef]

30. Janka, O.; Pöttgen, R. Reactive Fluxes. In *Handbook of Solid State Chemistry*; Dronskowski, R., Kikkawa, S., Stein, A., Eds.; Wiley-VCH: Weinheim, Germany, 2017.

31. Cotton, S. *Lanthanide and Actinide Chemistry*; John Wiley & Sons Ltd.: Chichester, England, 2006.

32. Cordero, B.; Gómez, V.; Platero-Prats, A.; Revés, M.; Echeverría, J.; Cremades, E.; Barragán, F.; Alvarez, S. Covalent radii revisited. *Dalton Trans.* **2008**, *2008*, 2832–2838. [CrossRef]

33. Steinberg, S.; Brgoch, J.; Miller, G.J.; Meyer, G. Identifying a Structural Preference in Reduced Rare-Earth Metal Halides by Combining Experimental and Computational Techniques. *Inorg. Chem.* **2012**, *51*, 11356–11364. [CrossRef]

34. Steinberg, S.; Card, N.; Mudring, A.-V. From the Ternary Eu(Au/In)$_2$ and EuAu$_4$(Au/In)$_2$ with Remarkable Au/In Distributions to a New Structure Type: The Gold-Rich Eu$_5$Au$_{16}$(Au/In)$_6$ Structure. *Inorg. Chem.* **2015**, *54*, 8187–8196. [CrossRef]
35. Smetana, V.; Steinberg, S.; Mudryk, Y.; Pecharsky, V.; Miller, G.J.; Mudring, A.-V. Cation-Poor Complex Metallic Alloys in Ba(Eu)-Au-Al(Ga) Systems: Identifying the Keys that Control Structural Arrangements and Atom Distributions at the Atomic Level. *Inorg. Chem.* **2015**, *54*, 10296–10308. [CrossRef]
36. Steinberg, S.; Dronskowski, R. The Crystal Orbital Hamilton Population (COHP) Method as a Tool to Visualize and Analyze Chemical Bonding in Intermetallic Compounds. *Crystals* **2018**, *8*, 225. [CrossRef]
37. Smetana, V.; Steinberg, S.; Mudring, A.-V. Layered Structures and Disordered Polyanionic Nets in the Cation-Poor Polar Intermetallics CsAu$_{1.4}$Ga$_{2.8}$ and CsAu$_2$Ga$_{2.6}$. *Cryst. Growth Des.* **2017**, *17*, 693–700. [CrossRef]
38. Davaasuren, B.; Dashjav, E.; Rothenberger, A. Synthesis and Characterization of the Ternary Telluroargentate K$_4$[Ag$_{18}$Te$_{11}$]. *Z. Anorg. Allg. Chem.* **2014**, *640*, 2939–2944. [CrossRef]
39. Jansen, M. Homoatomic d^{10}–d^{10} Interactions: Their Effects on Structure and Chemical and Physical Properties. *Angew. Chem. Int. Ed. Engl.* **1987**, *26*, 1098–1110. [CrossRef]
40. Pyykkö, P. Strong Closed-Shell Interactions in Inorganic Chemistry. *Chem. Rev.* **1997**, *97*, 597–636. [CrossRef]
41. Dreele, R.B.; Eyring, L.; Bowman, A.L.; Yamell, J.L. Refinement of the crystal structure of Pr$_7$O$_{12}$ by powder neutron diffraction. *Acta Crystallogr. Sect. B* **1975**, *31*, 971–974. [CrossRef]
42. Wang, R.; Steinfink, H.; Bradley, W.F. The crystal structure of lanthanum telluride and tellurium-deficient neodymium telluride. *Inorg. Chem.* **1966**, *5*, 142–145. [CrossRef]
43. Stöwe, K. Crystal structure, magnetic properties and band gap measurements of NdTe$_{(2−x)}$ (x = 0.11(1)). *Z. Kristallogr.* **2001**, *216*, 215–224. [CrossRef]
44. Adenis, C.; Langer, V.; Lindqvist, O. Reinvestigation of the structure of tellurium. *Acta Crystallogr. Sect. C* **1989**, *45*, 941–942. [CrossRef]
45. *WinXPow Version 2.23*; STOE & Cie GmbH: Darmstadt, Germany, 2008.
46. *Match! Vers. 3.8.0.137*; Crystal Impact GbR: Bonn, Germany, 2019.
47. *SAINT+ and SADABS*; Bruker AXS Inc.: Madison, WI, USA, 2009.
48. *XPREP, Version 6.03*; Bruker AXS Inc.: Madison, WI, USA, 2014.
49. Sheldrick, G.M. A short history of SHELX. *Acta Crystallogr. Sect. A Found. Crystallogr.* **2008**, *64*, 112–122. [CrossRef]
50. Sheldrick, G.M. Crystal structure refinement with SHELXL. *Acta Crystallogr. Sect. C Struct. Chem.* **2015**, *71*, 3–8. [CrossRef]
51. Blöchl, P.E. Projector augmented-wave method. *Phys. Rev. B Condens. Matter Mater. Phys.* **1994**, *50*, 17953–17979. [CrossRef]
52. Kresse, G.; Marsman, M.; Furthmüller, J. *Vienna Ab Initio Simulation Package (VASP), The Guide*; Computational Materials Physics, Faculty of Physics, Universität Wien: Vienna, Austria, 2014.
53. Kresse, G.; Furthmüller, J. Efficient iterative schemes for ab initio total-energy calculations using a plane-wave basis set. *Phys. Rev. B Condens. Matter Mater. Phys.* **1996**, *54*, 11169–11186. [CrossRef]
54. Kresse, G.; Furthmüller, J. Efficiency of ab-initio total energy calculations for metals and semiconductors using a plane wave basis set. *Comput. Mater. Sci.* **1996**, *6*, 15–50. [CrossRef]
55. Kresse, G.; Hafner, J. Ab initio molecular dynamics for liquid metals. *Phys. Rev. B Condens. Matter Mater. Phys.* **1993**, *47*, 558–561. [CrossRef]
56. Kresse, G.; Joubert, D. From ultrasoft pseudopotentials to the projector augmented-wave method. *Phys. Rev. B Condens. Matter Mater. Phys.* **1999**, *59*, 1758–1775. [CrossRef]
57. Perdew, J.P.; Burke, K.; Ernzerhof, M. Generalized Gradient Approximation Made Simple. *Phys. Rev. Lett.* **1996**, *77*, 3865–3868. [CrossRef]
58. Dronskowski, R.; Blöchl, P.E. Crystal Orbital Hamilton Populations (COHP). Energy-Resolved Visualization of Chemical Bonding in Solids Based on Density-Functional Calculations. *J. Phys. Chem.* **1993**, *97*, 8617–8624. [CrossRef]
59. Andersen, O.K. Linear methods in band theory. *Phys. Rev. B Condens. Matter Mater. Phys.* **1975**, *12*, 3060–3083. [CrossRef]
60. Andersen, O.K.; Jepsen, O. Explicit, First-Principles Tight-Binding Theory. *Phys. Rev. Lett.* **1984**, *53*, 2571–2574. [CrossRef]

61. Krier, G.; Jepsen, O.; Burkhardt, A.; Andersen, O.K. *TB-LMTO-ASA Program*, 4.7 ed.; Max-Planck-Institut für Festkörperforschung: Stuttgart, Germany, 1995.

62. von Barth, U.; Hedin, L. A local exchange-correlation potential for the spin polarized case: I. *J. Phys. C Solid State Phys.* **1972**, *5*, 1629–1642. [CrossRef]

63. Lambrecht, W.R.L.; Andersen, O.K. Minimal basis sets in the linear muffin-tin orbital method: Application to the diamond-stucture crystals C, Si, and Ge. *Phys. Rev. B Condens. Matter Mater. Phys.* **1986**, *34*, 2439–2449. [CrossRef]

64. Steinberg, S.; Bell, T.; Meyer, G. Electron Counting Rules and Electronic Structure in Tetrameric Transition-Metal (T)-Centered Rare-Earth (R) Cluster Complex Halides (X). *Inorg. Chem.* **2015**, *54*, 1026–1037. [CrossRef]

65. Bigun, I.; Steinberg, S.; Smetana, V.; Mudryk, Y.; Kalychak, Y.; Havela, L.; Pecharsky, V.; Mudring, A.-V. Magnetocaloric Behavior in Ternary Europium Indides EuT_5In: Probing the Design Capability of First-Principles-Based Methods on the Multifacted Magnetic Materials. *Chem. Mater.* **2017**, *29*, 2599–2614. [CrossRef]

66. Provino, A.; Steinberg, S.; Smetana, V.; Paramanik, U.; Manfrinetti, P.; Dhar, S.K.; Mudring, A.-V. Gold in the Layered Structures of $R_3Au_7Sn_3$: From Relativity to Versatility. *Cryst. Growth Des.* **2016**, *16*, 5657–5668. [CrossRef]

67. Li, W.-L.; Ertural, C.; Bogdanovski, D.; Li, J.; Dronskowski, R. Chemical Bonding of Crystalline LnB_6 (Ln = La–Lu) and Its Relationship with Ln_2B_8 Gas-Phase Complexes. *Inorg. Chem.* **2018**, *57*, 12999–13008. [CrossRef]

68. Blöchl, P.E.; Jepsen, O.; Andersen, O.K. Improved tetrahedron method for Brillouin-zone integrations. *Phys. Rev. B Condens. Matter Mater. Phys.* **1994**, *49*, 16223–16233. [CrossRef]